The Japan Society
of Fluid Mechanics

PAPER

Lift generation by a two-dimensional symmetric flapping wing: immersed boundary-lattice Boltzmann simulations

To cite this article: Keigo Ota *et al* 2012 *Fluid Dyn. Res.* **44** 045504

View the article online for updates and enhancements.

Related content

Recent citations

Lift generation by a two-dimensional symmetric flapping wing: immersed boundary-lattice Boltzmann simulations

Keigo Ota[1]**, Kosuke Suzuki**[1] **and Takaji Inamuro**[1,2]

[1] Department of Aeronautics and Astronautics, Graduate School of Engineering, Kyoto University, Kyoto 606-8501, Japan
[2] Advanced Research Institute of Fluid Science and Engineering, Graduate School of Engineering, Kyoto University, Kyoto 615-8530, Japan

E-mail: inamuro@kuaero.kyoto-u.ac.jp

Abstract

Two-dimensional (2D) symmetric flapping flight is investigated by an immersed boundary-lattice Boltzmann method (IB-LBM). In this method, we can treat the moving boundary problem efficiently on the Cartesian grid. We consider a model consisting of 2D symmetric flapping wings without mass connected by a hinge with mass. Firstly, we investigate the effect of the Reynolds number in the range of 40–200 on flows around symmetric flapping wings under no gravity field and find that for high Reynolds numbers ($Re \geqslant 55$), asymmetric vortices with respect to the horizontal line appear and the time-averaged lift force is induced on the wings, whereas for low Reynolds numbers ($Re \leqslant 50$), only symmetric vortices appear around the wings and no lift force is induced. Secondly, the effect of the initial position of the wings is investigated, and the range of the initial phases where the upward flight is possible is found. The effects of the mass and flapping amplitude are also studied. Finally, we carry out free flight simulations under gravity field for various Reynolds numbers in the range $60 \leqslant Re \leqslant 300$ and Froude numbers in the range $3 \leqslant Fr \leqslant 60$ and identify the region where upward flight is possible.

(Some figures may appear in colour only in the online journal)

1. Introduction

The flapping flight of tiny insects is of fundamental interest not only in biology itself but also in its practical use related to the development of micro-air vehicles (MAVs). It has

been pointed out that a leading edge vortex (LEV) created around wings plays an important role in the generation of the lift force, and several lift-generating mechanisms have been proposed (e.g. Sane 2003, Wang 2005). Not only three-dimensional (3D) wings but also 2D wings are used for theoretical and numerical investigations. As to the 2D investigations, most approaches deal with a wing with a high aspect ratio (a wing with infinite spanwise length). For example, Miller and Peskin (2004) investigated the LEV around a 2D wing during one complete stroke for Reynolds numbers between 8 and 128. They observed the aerodynamic transition at critical Reynolds number between 32 and 64. Vandenberghe *et al* (2004) and Alben and Shelley (2005) studied flapping flight by the heaving motion of a wing experimentally and numerically, respectively, and found that the wing begins to move forward spontaneously due to a symmetry-breaking bifurcation as the Reynolds number based on the flapping frequency exceeds a critical value. On the other hand, a wing with infinite chordwise length (an infinitely long insect) has also been used. For instance, Iima and Yanagita (2001a,b, 2005, 2006) investigated a 2D symmetric flapping wing with infinite chordwise length. Although the motions of the 2D wings with high aspect ratio and with infinite chordwise length are quite different, there are common features of vortex dynamics around the wing in flapping motion for force generation, such as vortex shedding from a leading edge, interaction and dissipation of vortices and symmetry breaking of vorticity.

For a 2D symmetric flapping wing, it is believed that no mean lift force is generated by the wing, since the upward force generated during the downstroke is canceled by the downward force during upstroke. However, Iima and Yanagita (2001a,b, 2005, 2006) applied the discrete vortex method for inviscid fluid flows to the simulation of the flow around a 2D symmetric flapping wing with infinite chordwise length and found that the generation of lift is possible by the symmetry breaking of flows. In their method, fluid viscosity is approximately introduced by the core-spreading method in which the radius of a vortex blob increases with the time elapsed since its creation and diverges to infinity when the elapsed time exceeds a critical value and thus the Reynolds number of the flows cannot be defined in their approach. Therefore, the effect of Reynolds number on symmetry breaking is not so clear quantitatively.

From the viewpoint of numerical simulations, the flapping wing is a typical example of moving boundary problems. Body-fitted or unstructured-grid methods have commonly been used to simulate the moving boundary problems. However, the algorithms of the methods are generally complicated, and the computational costs of the methods are high. In recent years various immersed boundary methods (IBMs) have been proposed to simulate flows with moving boundaries in the Cartesian grid (e.g. Mittal and Iaccarino 2005). The IBM is a simple approach to the moving boundary problems, although some techniques are required to satisfy the no-slip boundary condition at the moving boundary. In addition, the lattice Boltzmann method (LBM) has been developed into an alternative and promising numerical scheme for simulating viscous fluid flows in the Cartesian grid without solving the Poisson equation for pressure field (e.g. Succi 2001). Since both of the above methods are based on the Cartesian grid, the LBM combined with the IBM (so-called IB-LBM) is well suited to simulations of moving boundary problems, and several approaches of the IB-LBM have already been presented (e.g. Feng and Michaelides 2005, Shu *et al* 2007). The authors also proposed a new IB-LBM (Suzuki and Inamuro 2011), which is more accurate for satisfying the no-slip boundary condition at a moving boundary than other IB-LBMs.

In this paper, we apply the IB-LBM (Suzuki and Inamuro 2011) to the investigations of flows and lift generation by the 2D symmetric flapping wing proposed by Iima and Yanagita (2001a,b, 2005, 2006). The paper is organized as follows. In section 2, a model of 2D flapping wings is explained. The governing equations are described in section 3, and numerical methods are presented in section 4. In section 5, we investigate the effects of the Reynolds
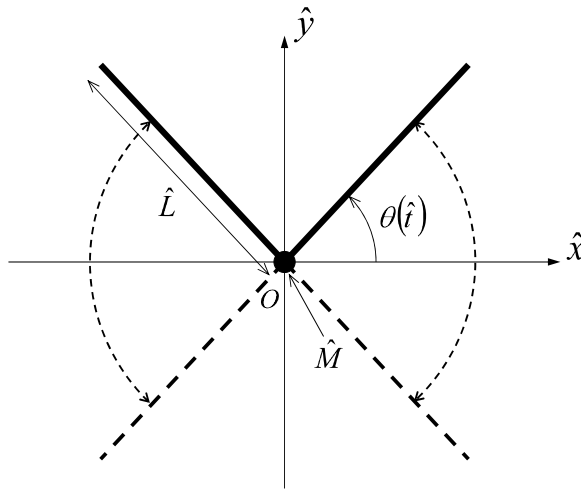
Figure 1. The 2D flapping wing.

number, initial positions of the wings, the mass of the model and flapping amplitudes on flapping flight under no-gravity. Also, flapping flight under gravity is investigated for various Reynolds numbers and Froude numbers. Finally, the conclusions are given in section 6.

2. The 2D symmetric flapping wing

A model of a 2D symmetric flapping wing is shown in figure 1. Each of the two wings is composed of a straight line with the length of $\hat{L}$ and no mass. The body located between both the wings is made up of a point particle with the mass of $\hat{M}$. The model is basically the same as that of Iima and Yanagita (2001a,b, 2005, 2006) except that in their model the root of the wing and the body are a short distance apart. The wings flap symmetrically with respect to the vertical and horizontal lines. The angular position $\theta(\hat{t})$ at time $\hat{t}$ of a harmonic oscillation of the wing is given by

$$\theta(\hat{t}) = \Delta\theta \cos\left(\frac{2\pi}{\hat{T}}\hat{t} + \frac{\phi}{180}\pi\right), \tag{2.1}$$

where $\Delta\theta$, $\hat{T}$ and ϕ are the amplitude, period and initial phase of the oscillation, respectively. Note that for $\phi = 0°$ the wing is initially located at the most upward position. Also, the initial position and velocity of the wings are symmetric with respect to the vertical line, but asymmetric with respect to the horizontal line for any value of ϕ. That is, the motion of the wings has an initial vertical directionality.

The tip velocity $\hat{u}_{\mathrm{tip}}$ of the wing is obtained by

$$\hat{u}_{\mathrm{tip}} = \hat{L}\frac{\mathrm{d}\theta}{\mathrm{d}\hat{t}}, \tag{2.2}$$

and the time-averaged tip speed $\overline{\hat{u}}_{\mathrm{tip}}$ of the wing is obtained by

$$\overline{\hat{u}}_{\mathrm{tip}} = \frac{1}{\hat{T}}\int_0^{\hat{T}}|\hat{u}_{\mathrm{tip}}|\mathrm{d}\hat{t} = \frac{4\hat{L}\Delta\theta}{\hat{T}}. \tag{2.3}$$

3. The governing equation

In this section, we use the non-dimensional variables defined by (A.1) in appendix A. We consider incompressible viscous fluid flows governed by the continuity equation and the Navier–Stokes equations as follows:

$$\nabla \cdot \boldsymbol{u} = 0, \tag{3.1}$$

$$\frac{\mathrm{D}\boldsymbol{u}}{\mathrm{D}t} = -\nabla p + \frac{1}{Re}\nabla^2 \boldsymbol{u}, \tag{3.2}$$

where $\boldsymbol{u}$ is the fluid velocity and p is the pressure, and Re is the Reynolds number defined by

$$Re = \frac{\overline{\hat{u}}_{\text{tip}}\hat{L}}{\hat{v}}, \tag{3.3}$$

where $\hat{v}$ is the kinematic viscosity of the fluid.

On the other hand, as to the motion of the body with the wings we consider the motion in the x- and y-directions, but ignore the rotation of the body. That is, the center of mass $\boldsymbol{X}_{\text{c}}$ moves by Newton's law as follows:

$$M\frac{\mathrm{d}\boldsymbol{U}_{\text{c}}}{\mathrm{d}t} = \boldsymbol{F} + M\boldsymbol{G}, \tag{3.4}$$

$$\frac{\mathrm{d}\boldsymbol{X}_{\text{c}}}{\mathrm{d}t} = \boldsymbol{U}_{\text{c}}, \tag{3.5}$$

where M is the mass, $\boldsymbol{U}_{\text{c}}$ is the velocity of the center of mass, $\boldsymbol{F}$ is the force acting on the wings, and $\boldsymbol{G} = (0, -G)$ is the gravity acceleration. G is related to the Froude number defined by

$$Fr = \frac{1}{\sqrt{G}} = \frac{\overline{\hat{u}}_{\text{tip}}}{\sqrt{\hat{G}\hat{L}}}, \tag{3.6}$$

where $\hat{G}$ is the dimensional gravity acceleration.

It is noted that the dimensionless parameters of the present problem are the Reynolds number Re, the Froude number Fr and the non-dimensional mass M. To solve the above equations (3.1)–(3.5), we need initial conditions for $\boldsymbol{u}$, $\boldsymbol{X}_{\text{c}}$ and $\boldsymbol{U}_{\text{c}}$ as well as the no-slip boundary condition on the wings for $\boldsymbol{u}$.

4. Numerical method

We use an IB-LBM to solve (3.1)–(3.3). The motion of the body with the wings determined by (3.4) and (3.5) is computed by the second-order Adams–Bashforth method. At each time step the force acting on the wing is computed, and then the motion of the body is explicitly updated. Non-dimensional variables are defined by (A.2) in appendix A.

4.1. The LBM

In the LBM, a modeled gas, which is composed of identical particles whose velocities are restricted to a finite set of vectors, is considered (e.g. Succi 2001). The 2D lattice with nine velocity vectors, the so-called D2Q9 model, is used in the present study. The D2Q9 model has the velocity vectors $\boldsymbol{c}_i = (0, 0), (0, \pm 1), (\pm 1, 0), (\pm 1, \pm 1)$ for $i = 1, 2, \ldots, 9$. The evolution of the particle distribution function $f_i(\boldsymbol{x}, t)$ with the velocity $\boldsymbol{c}_i$ at the point $\boldsymbol{x}$ and time t is

computed by the following equations:

$$f_i(\boldsymbol{x} + \boldsymbol{c}_i \Delta x, t + \Delta t) - f_i(\boldsymbol{x}, t) = -\frac{1}{\tau}[f_i(\boldsymbol{x}, t) - f_i^{\mathrm{eq}}(\boldsymbol{x}, t)], \tag{4.1}$$

where Δx is a lattice spacing, Δt is a time step, f_i^{eq} is an equilibrium distribution function, and τ is a single relaxation time of $O(1)$. It is noted that Δt is chosen so that the particles travel one lattice spacing during the time step. Note that $\Delta t = Sh \Delta x$ where $Sh = \hat{L}/(\hat{t}_0 \hat{c}) = \bar{\hat{u}}_{\mathrm{tip}}/\hat{c} = O(\Delta x)$ in the diffusive time scale $\hat{t}_0 = \hat{L}/\bar{\hat{u}}_{\mathrm{tip}}$ ($\hat{c}$ is a characteristic particle speed). The equilibrium distribution function f_i^{eq} is given by

$$f_i^{\mathrm{eq}} = E_i \rho \left[1 + 3\boldsymbol{c}_i \cdot \boldsymbol{u} + \tfrac{9}{2}(\boldsymbol{c}_i \cdot \boldsymbol{u})^2 - \tfrac{3}{2}\boldsymbol{u} \cdot \boldsymbol{u} \right], \tag{4.2}$$

where $E_1 = 4/9$, $E_2 = E_3 = E_4 = E_5 = 1/9$, and $E_6 = E_7 = E_8 = E_9 = 1/36$. The density ρ and the fluid velocity $\boldsymbol{u}$ are calculated in terms of the particle distribution function by

$$\rho = \sum_{i=1}^{9} f_i, \tag{4.3}$$

$$\boldsymbol{u} = \frac{1}{\rho} \sum_{i=1}^{9} f_i \boldsymbol{c}_i. \tag{4.4}$$

Note that we assume that $\boldsymbol{u} = O(\Delta x)$. The pressure p is related to the density by

$$p = \tfrac{1}{3}\rho. \tag{4.5}$$

It is found that the asymptotic expansions of $\boldsymbol{u}$ and p with respect to Δx can be expressed by $\boldsymbol{u} = (\Delta x)\boldsymbol{u}^{(1)} + (\Delta x)^2 \boldsymbol{u}^{(2)} + (\Delta x)^3 \boldsymbol{u}^{(3)} + \cdots$ and $p = 1/3 + (\Delta x)^2 p^{(2)} + (\Delta x)^3 p^{(3)} + (\Delta x)^4 p^{(4)} + \cdots$, and $\boldsymbol{u}^{(1)}$ and $p^{(2)}$ satisfy the continuity equation (3.1) and the Navier–Stokes equations (3.2) for an incompressible viscous fluid with the kinematic viscosity ν given by

$$\nu = \tfrac{1}{3}\left(\tau - \tfrac{1}{2}\right)\Delta x, \tag{4.6}$$

while $\boldsymbol{u}^{(2)}$ and $p^{(3)}$ are zero with appropriate initial and boundary conditions (Inamuro 2006, Junk *et al* 2005). That is, the solutions to (4.1)–(4.15) give the pressure and the velocities for incompressible viscous fluid flows with relative errors of $O[(\Delta x)^2]$. The errors come from the compressibility of fluid flows in the LBM.

The no-slip boundary condition on the wings is satisfied with the body force $\boldsymbol{g}(\boldsymbol{x}, t)$, which is obtained by the immersed boundary method described below. In order to include the body force $\boldsymbol{g}(\boldsymbol{x}, t)$ into the LBM, the evolution equation (4.1) is split into the following two steps:

$$f_i^*(\boldsymbol{x} + \boldsymbol{c}_i \Delta x, t + \Delta t) = f_i(\boldsymbol{x}, t) - \frac{1}{\tau}[f_i(\boldsymbol{x}, t) - f_i^{\mathrm{eq}}(\boldsymbol{x}, t)], \tag{4.7}$$

$$f_i(\boldsymbol{x}, t + \Delta t) = f_i^*(\boldsymbol{x}, t + \Delta t) + 3E_i \rho^*(\boldsymbol{x}, t + \Delta t)\boldsymbol{c}_i \cdot \boldsymbol{g}(\boldsymbol{x}, t + \Delta t)\Delta x. \tag{4.8}$$

4.2. The projection-lattice Boltzmann method (PLBM)

As described above, the LBM is the second-order accurate method for incompressible viscous fluid flows and has compressibility errors of higher-order expansions which are distinguished in the early stage of flapping. In order to reduce the compressibility errors, we use the PLBM proposed by Inamuro *et al* (2004) only in the early stage of flapping. In the PLBM, we can

obtain the pressure field satisfying the continuity equation by solving the Poisson equation. The evolution equations are given by

$$f_i^\dagger(\boldsymbol{x} + \boldsymbol{c}_i \Delta x, t + \Delta t) = f_i(\boldsymbol{x}, t) - \frac{1}{\tau}[f_i(\boldsymbol{x}, t) - f_i^{\text{eq}}(\boldsymbol{x}, t)], \tag{4.9}$$

$$f_i^*(\boldsymbol{x}, t + \Delta t) = f_i^\dagger(\boldsymbol{x}, t + \Delta t) - 3E_i \boldsymbol{c}_i \cdot \nabla p(\boldsymbol{x}, t + \Delta t) \Delta x, \tag{4.10}$$

The equilibrium distribution function f_i^{eq} in (4.9) is slightly different from (4.2), i.e. the density ρ is removed:

$$f_i^{\text{eq}} = E_i \left[1 + 3\boldsymbol{c}_i \cdot \boldsymbol{u} + \tfrac{9}{2}(\boldsymbol{c}_i \cdot \boldsymbol{u})^2 - \tfrac{3}{2}\boldsymbol{u} \cdot \boldsymbol{u} \right], \tag{4.11}$$

where the velocity $\boldsymbol{u}$ is defined by

$$\boldsymbol{u} = \sum_{i=1}^{9} f_i \boldsymbol{c}_i. \tag{4.12}$$

The pressure p in (4.10) is obtained by solving the following Poisson equation:

$$\nabla^2 p(\boldsymbol{x}, t + \Delta t) = Sh \frac{\nabla \cdot \boldsymbol{u}^\dagger(\boldsymbol{x}, t + \Delta t)}{\Delta t}. \tag{4.13}$$

The Poisson equation is computed by using the Jacobi method, which is the simplest iterative method. The iteration is repeated until $|p_{n+1} - p_n| < 10^{-9}$ (where n is the number of iterations) is satisfied in the whole domain. As a matter of course, the computation time by the PLBM is much larger than that by the LBM.

4.3. Immersed boundary method

The idea of the IBM was originally proposed by Peskin (1972) to simulate flows around flexible membranes in the Cartesian grid, and various IBMs have been proposed later by Mittal and Iaccarino (2005). In this paper, we use the IBM proposed by Wang *et al* (2008).

Supposing that $f_i(\boldsymbol{x}, t)$, $\boldsymbol{u}(\boldsymbol{x}, t)$ and $p(\boldsymbol{x}, t)$ are known, the temporal $f_i^*(\boldsymbol{x}, t + \Delta t)$ and $\boldsymbol{u}^*(\boldsymbol{x}, t + \Delta t)$ can be calculated by (4.7) and (4.4), respectively. Let $\boldsymbol{X}_k(t + \Delta t)$ and $\boldsymbol{U}_k(t + \Delta t)(k = 1, 2, \ldots, N)$ be the Lagrangian points of the moving boundary and the boundary velocities at the points, respectively. Note that the moving boundary is represented by N points, and the Lagrangian points $\boldsymbol{X}_k$ generally differ from the Eulerian grid points $\boldsymbol{x}$. Then, the temporal velocities $\boldsymbol{u}^*(\boldsymbol{X}_k, t + \Delta t)$ at the Lagrangian points $\boldsymbol{X}_k$ are interpolated by

$$\boldsymbol{u}^*(\boldsymbol{X}_k, t + \Delta t) = \sum_{\boldsymbol{x}} \boldsymbol{u}^*(\boldsymbol{x}, t + \Delta t) \, W(\boldsymbol{x} - \boldsymbol{X}_k)(\Delta x)^2, \tag{4.14}$$

where $\sum_{\boldsymbol{x}}$ indicates the sum of all the Eulerian grid points, and the weight function W is given by Lai and Peskin (2000):

$$W(x, y) = \frac{1}{\Delta x} w\left(\frac{x}{\Delta x}\right) \cdot \frac{1}{\Delta x} w\left(\frac{y}{\Delta x}\right) \tag{4.15}$$

and

$$w(r) = \begin{cases} \frac{1}{8}\left(3 - 2|r| + \sqrt{1 + 4|r| - 4r^2}\right), & |r| \leqslant 1, \\ \frac{1}{8}\left(5 - 2|r| - \sqrt{-7 + 12|r| - 4r^2}\right), & 1 \leqslant |r| \leqslant 2, \\ 0, & \text{otherwise.} \end{cases} \tag{4.16}$$

The body force $\boldsymbol{g}(\boldsymbol{x}, t + \Delta t)$ is determined by the following iterative procedure.

Step 0. Compute the initial value of the body force at the Lagrangian points by

$$\boldsymbol{g}_0(\boldsymbol{X}_k, t + \Delta t) = Sh \frac{\boldsymbol{U}_k(t + \Delta t) - \boldsymbol{u}^*(\boldsymbol{X}_k, t + \Delta t)}{\Delta t}, \tag{4.17}$$

where it is noted that $Sh/\Delta t = 1/\Delta x$ as defined in section 4.1.

Step 1. Compute the body force at the Eulerian grid points of the lth iteration by

$$\boldsymbol{g}_l(\boldsymbol{x}, t + \Delta t) = \sum_{k=1}^{N} \boldsymbol{g}_l(\boldsymbol{X}_k, t + \Delta t) W(\boldsymbol{x} - \boldsymbol{X}_k) \Delta S, \tag{4.18}$$

where $\Delta S = \Delta x \times s$ (s is the length of the Lagrangian grid).

Step 2. Correct the velocity at the Eulerian grid point by

$$\boldsymbol{u}_l(\boldsymbol{x}, t + \Delta t) = \boldsymbol{u}^*(\boldsymbol{x}, t + \Delta t) + \boldsymbol{g}_l(\boldsymbol{x}, t + \Delta t) \Delta t / Sh. \tag{4.19}$$

Step 3. Interpolate the velocity at the Lagrangian point with

$$\boldsymbol{u}_l(\boldsymbol{X}_k, t + \Delta t) = \sum_{\boldsymbol{x}} \boldsymbol{u}_l(\boldsymbol{x}, t + \Delta t) \, W(\boldsymbol{x} - \boldsymbol{X}_k)(\Delta x)^2. \tag{4.20}$$

Step 4. Correct the body force with

$$\boldsymbol{g}_{l+1}(\boldsymbol{X}_k, t + \Delta t) = \boldsymbol{g}_l(\boldsymbol{X}_k, t + \Delta t) + Sh \frac{\boldsymbol{U}_k(t + \Delta t) - \boldsymbol{u}_l(\boldsymbol{X}_k, t + \Delta t)}{\Delta t} \tag{4.21}$$

and go to step 1.

From preliminary computations, we found that $\boldsymbol{g}_{l=4}(\boldsymbol{x}, t + \Delta t)$ is enough to keep the no-slip boundary condition at the wings; the point-averaged error of $|\boldsymbol{U}_k(t + \Delta t) - \boldsymbol{u}_{l=4}(\boldsymbol{X}_k, t + \Delta t)|/\overline{u}_{\text{tip}}$ is less than 0.5%. Therefore, we iterate the above procedure until $l = 4$ in the following computations.

4.4. Motion of the body with flapping wings

The motion of the body with the wings can be calculated by Newton's law (3.4) and (3.5). First, the force acting on the wings $\boldsymbol{F}$ is obtained by Lai and Peskin (2000):

$$\boldsymbol{F}(t) = - \sum_{\boldsymbol{x}} \boldsymbol{g}(\boldsymbol{x}, t)(\Delta x)^2. \tag{4.22}$$

Then, the second-order Adams–Bashforth method is used for computing (3.4) and (3.5) as follows:

$$\boldsymbol{U}_{\text{c}}(t + \Delta t) = \boldsymbol{U}_{\text{c}}(t) + \frac{1}{M} \left[\frac{3}{2} \boldsymbol{F}(t) - \frac{1}{2} \boldsymbol{F}(t - \Delta t) \right] \frac{\Delta t}{Sh} + \boldsymbol{G} \frac{\Delta t}{Sh}, \tag{4.23}$$

$$\boldsymbol{X}_{\text{c}}(t + \Delta t) = \boldsymbol{X}_{\text{c}}(t) + \left[\frac{3}{2} \boldsymbol{U}_{\text{c}}(t) - \frac{1}{2} \boldsymbol{U}_{\text{c}}(t - \Delta t) \right] \frac{\Delta t}{Sh}, \tag{4.24}$$

where at $t = 0$ we assume that $\boldsymbol{F}(-\Delta t) = \boldsymbol{F}(0)$ and $\boldsymbol{U}_{\text{c}}(-\Delta t) = \boldsymbol{U}_{\text{c}}(0)$, i.e. the first-order Euler method is used at $t = 0$.

4.5. Algorithm of computation

The algorithm of computation by the present IB-LBM is summarized as follows.

Step 0.　Suppose the initial value of $f_i(\boldsymbol{x}, 0)$ and compute $\boldsymbol{u}(\boldsymbol{x}, 0)$ and $p(\boldsymbol{x}, 0)$ by (4.3)–(4.5) and $\boldsymbol{F}(0)$ by (4.22). Also, assign $\boldsymbol{X}_{\mathrm{c}}(0)$ and $\boldsymbol{U}_{\mathrm{c}}(0)$.

Step 1.　Compute $\boldsymbol{U}_{\mathrm{c}}(t + \Delta t)$ and $\boldsymbol{X}_{\mathrm{c}}(t + \Delta t)$ by (4.23) and (4.24), and $\boldsymbol{U}_k(t + \Delta t)$ and $\boldsymbol{X}_k(t + \Delta t)$ with (2.1).

Step 2.　Compute $f_i^*(\boldsymbol{x}, t + \Delta t)$ by (4.7) with (4.2) and $\boldsymbol{u}^*(\boldsymbol{x}, t + \Delta t)$ by (4.4). Then compute $\boldsymbol{u}^*(\boldsymbol{X}_k, t + \Delta t)$ by (4.14).

Step 3.　Compute $\boldsymbol{g}(\boldsymbol{x}, t + \Delta t)$ by (4.14)–(4.21) with $l = 4$ and $\boldsymbol{F}(t + \Delta t)$ by (4.22).

Step 4.　Compute $f_i(\boldsymbol{x}, t + \Delta t)$ by (4.8), and $\boldsymbol{u}(\boldsymbol{x}, t + \Delta t)$ and $p(\boldsymbol{x}, t + \Delta t)$ by (4.3)–(4.5).

Step 5.　Advance one time step and return to step 1.

On the other hand, the algorithm of computation by the IB-PLBM should be changed in step 2 as follows:

Step 2.　Compute $f_i^*(\boldsymbol{x}, t + \Delta t)$ by (4.9) and (4.10) with (4.11)–(4.13), and $\boldsymbol{u}^*(\boldsymbol{x}, t + \Delta t)$ by (4.4). Then compute $\boldsymbol{u}^*(\boldsymbol{X}_k, t + \Delta t)$ by (4.14).

4.6. Accuracy of the method

In order to examine the accuracy of the present method, we have calculated typical flows with moving boundaries: an oscillating circular cylinder, an impulsively moving circular cylinder and an almost impulsively moving plate. The results agree very well with other numerical results as shown in appendix B.

5. Results and discussion

5.1. Computational conditions

In the following computations, in order to reduce the compressibility errors in the early stage we use the combination of the IB-PLBM and IB-LBM, i.e. the IB-PLBM is used for $0 < t/T \leqslant 1$ and the IB-LBM is used for $t/T \geqslant 1$, and at $t/T = 1$ the final results by the IB-PLBM are transferred into the initial data for the IB-LBM. The differences between the results of the IB-LBM, the IB-PLBM and the combination of the IB-PLBM and IB-LBM are shown in appendix C.

The computational domain is shown in figure 2. The width and height of the domain are $W = 12L$ and $H = 24L$, respectively. The bounce-back boundary condition (e.g. Succi 2001) is imposed on the walls of the domain. The body equipped with the flapping wings is initially placed at the center of the domain filled with a stationary fluid. In the following, computations are performed for various Reynolds numbers of $Re \leqslant 300$ and various Froude numbers with the specific values of $M = 9.05$ and $\Delta\theta = 2\pi \times 0.13 (= 46.8^\circ)$, which are the same as in Iima and Yanagita (2005).

We have carried out preliminary computations in order to test the influence of grid resolution and found the following necessary grids (see appendix D). For $40 \leqslant Re \leqslant 150$, we use the Eulerian grid of $W \times H = 720\Delta x \times 1440\Delta x$ and the Lagrangian grid of $L = 60\Delta x$. For $150 < Re \leqslant 200$, we use $W \times H = 960\Delta x \times 1920\Delta x$ and $L = 80\Delta x$, and for $200 < Re \leqslant 300$, we use $W \times H = 1440\Delta x \times 2880\Delta x$ and $L = 120\Delta x$. Other computational conditions are listed in table E.1 in appendix E. In addition, the effect of the domain size was investigated, and it has been confirmed that the domain sizes in the range of $8L \leqslant W \leqslant 16L$ and $16L \leqslant H \leqslant 32L$ have almost no effect on the following results (see appendix F).
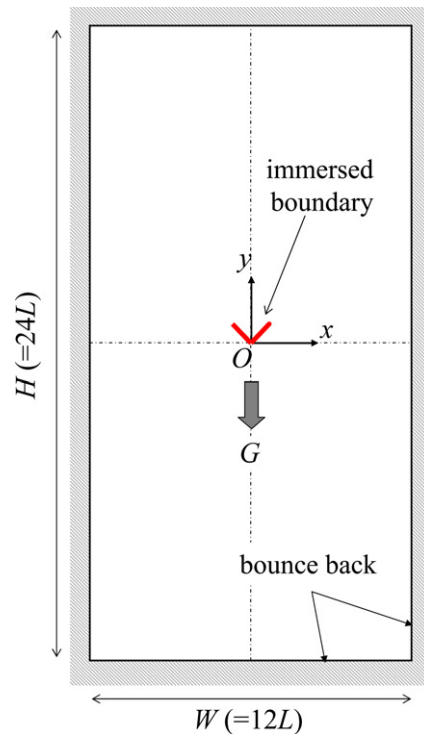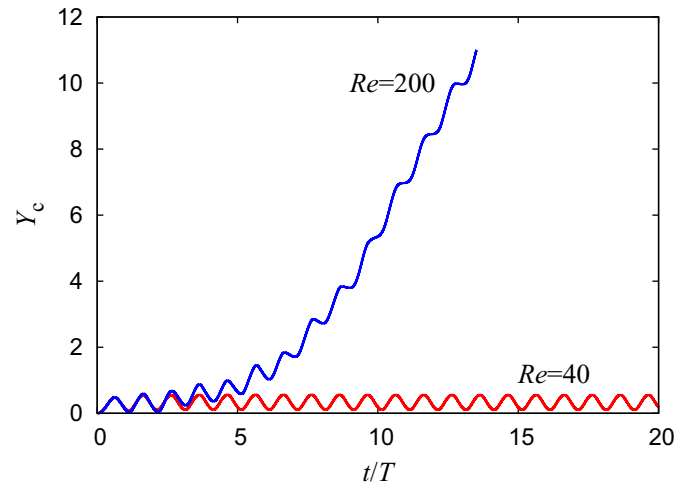
Figure 2. Computational domain.

Figure 3. Trajectories of Y_c (the y-position of the center of mass) at $Re = 40$ and 200 with $\phi = 0°$ under no gravity.

5.2. Flapping flight under no gravity

5.2.1. Effect of Reynolds number   First, we compute flapping flight under no gravity ($G = 0$ or $Fr = \infty$). The initial phase ϕ of the flapping in (2.1) is set at $\phi = 0°$, which means that the wings are initially located at the most upward position. Figure 3 shows the trajectory of
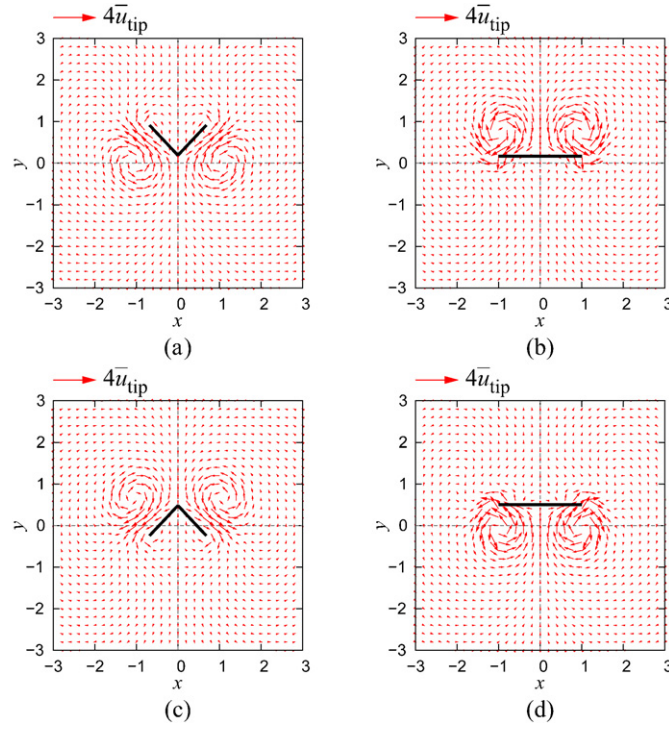
Figure 4. Velocity vectors around flapping wings under no gravity at $Re = 40$ with $\phi = 0°$. (a) $t/T = 6.0$, (b) $t/T = 6.25$, (c) $t/T = 6.5$ and (d) $t/T = 6.75$. The velocity vectors are drawn at every nine lattice.

Y_c (the y-position of the center of mass) at $Re = 40$ and 200. It is found that at $Re = 200$ the body goes upward after two strokes, while at $Re = 40$ the body moves up and down around a position of $y > 0$. Also, it is noted that the body goes upward during the first half stroke of the wings for both Re, because the force acting on the wings is positive during that time.

The flow fields at $Re = 40$ and 200 are shown in figures 4 and 5, respectively. The figures show velocity vectors around the flapping wings during one stroke for the seventh period from $t = 0$. As described in section 1, it is found that LEVs are created around the wings and the LEVs play an important role in flapping flight. In addition, it is seen from figure 4 that when the wings are in symmetrical positions with respect to the horizontal line, i.e. (a) ↔ (c) and (b) ↔ (d) in the figure, the flow fields are symmetric with respect to the horizontal line. On the other hand, it is seen from figure 5 that at $Re = 200$ the flow fields are not symmetric with respect to the horizontal line, even when the wings are in symmetrical positions. That is, the symmetry breaking of the flows appears at $Re = 200$. In addition, it is found that a pair of vortices stays under the wings for all time during the period, and a weak downward jet appears below the vortices. The downward jet is balanced by the upward motion of the body.

Figure 6 shows the time evolution of the y-component force F_y defined by (A.1) at $Re = 40$ and 200. As seen in the figure, at $Re = 40$ the force changes periodically after three strokes, while at $Re = 200$ the force does not change periodically. As seen in figures 6(a) and (b), the magnitude of the positive peak is smaller than that of the negative peak at $Re = 200$, but the time-averaged force becomes positive for $2 \leqslant t/T \leqslant 9$, which means that the area of positive forces is larger than the area of negative forces, and the body is accelerated upward
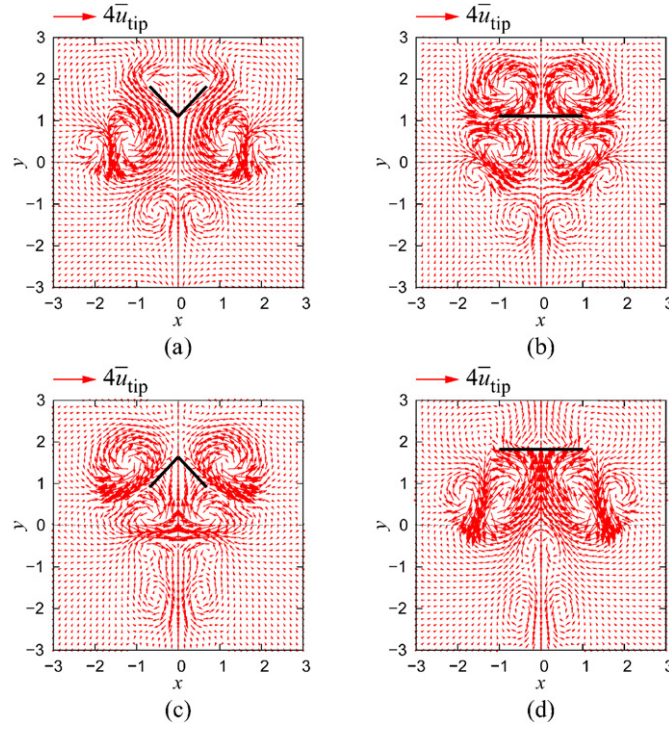
Figure 5. Velocity vectors around flapping wings under no gravity at $Re = 200$ with $\phi = 0^\circ$. (a) $t/T = 6.0$, (b) $t/T = 6.25$, (c) $t/T = 6.5$ and (d) $t/T = 6.75$. The velocity vectors are drawn at every 12 lattice.

during those strokes. In addition, it is noted that as seen in figures 4 and 5, the flow field is symmetry at $x = 0$, and hence $F_x = 0$ and $X_c = 0$ for all time at $Re = 40$ and 200.

From the above-described results, it is expected that the symmetry breaking of flows with respect to the horizontal line occurs between $Re = 40$ and 200. In order to find the critical Reynolds number over which the symmetry breaking occurs, we compute flapping flight under no gravity ($G = 0$ or $Fr = \infty$) with the same initial condition $\phi = 0^\circ$ for various Reynolds numbers between $Re = 40$ and 200. As described in section 2, the initial condition ($\phi = 0^\circ$) is not symmetric with respect to the horizontal line. That is, the system initially has a vertical directionality. It is also noted that the effect of the initial condition decays for viscous flows. In addition, it is expected that near the critical Reynolds number, the flow is sensitive to disturbance. Therefore, several disturbances are applied to the motion of wings. The computed results are shown in figure 7. In the figure, 'Disturbance ($\alpha\% @ t/T = \beta$)' means a disturbance such that the downstroke is speeded up by $\alpha\%$ during $\beta - 1 \leqslant t/T \leqslant \beta - 0.5(1 + 0.01\alpha)$. It is seen from figure 7 that for $Re \leqslant 50$ the body stays at an equilibrium position in spite of the disturbances, while for $55 \leqslant Re \leqslant 110$ the body goes either upward or downward depending on the disturbances. It is noted that the body goes only upward for $Re \geqslant 65$ in the case of no disturbance, and from this result we find that the initial condition ($\phi = 0^\circ$) determines the upward direction of the motion. The body goes upward by the disturbance which speeds up the downstroke ($\alpha > 0$) and goes downward by the disturbance which slows down the downstroke ($\alpha < 0$), and as α (< 0) decreases, the region of Re where the body goes downward is extended. As a result, we have the bistable phenomena for $55 \leqslant Re \leqslant 110$ where the effect of the disturbances with $\alpha < 0$ overcomes that of the initial condition. For
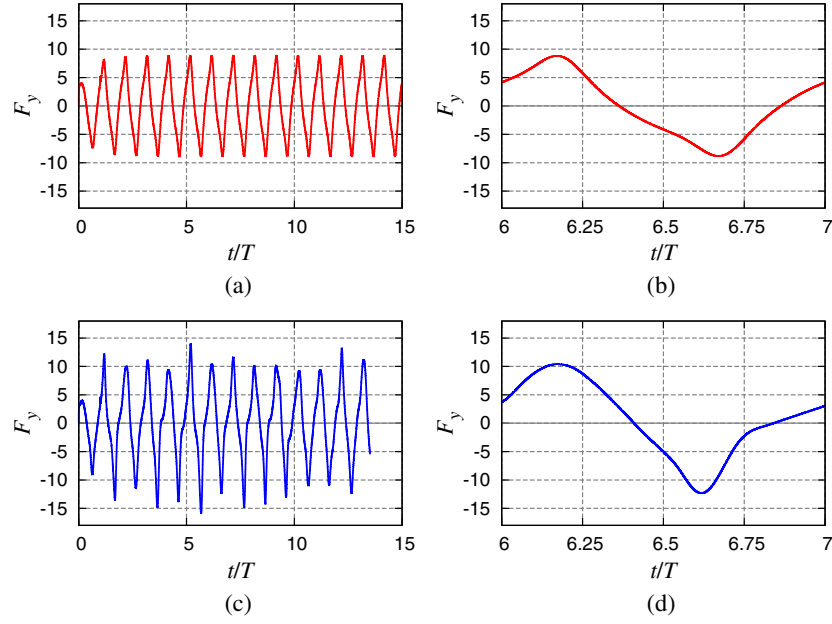
Figure 6. Time evolution of dimensionless force F_y under no gravity with $\phi = 0°$ for (a) $0 < t/T \leqslant 15$, (b) $6 \leqslant t/T \leqslant 7$ at $Re = 40$, and for (c) $0 < t/T \leqslant 13.5$, (d) $6 \leqslant t/T \leqslant 7$ at $Re = 200$.
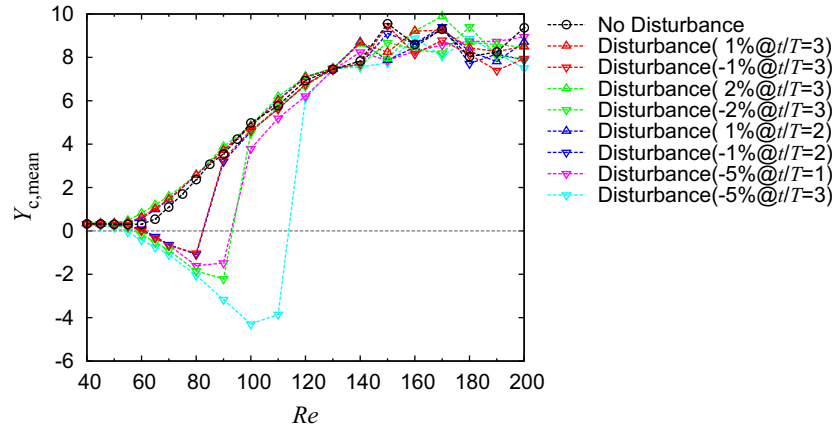

Figure 7. Time-averaged position $Y_{c,mean}$ for $12 \leqslant t/T \leqslant 13$ against various Reynolds numbers under no gravity with $\phi = 0°$. 'Disturbance ($\alpha\%@t/T = \beta$)' means a disturbance such that the downstroke is speeded up by $\alpha\%$ during $\beta - 1 \leqslant t/T \leqslant \beta - 0.5(1 + 0.01\alpha)$.

$Re \geqslant 120$, however, the body goes upward in spite of the disturbances, since the effect of the initial condition overcomes that of the disturbances.

It is interesting that the Reynolds number ($Re \approx 50$) where the symmetry breaking appears is similar to that ($32 < Re < 64$) of Miller and Peskin (2004), although the motions of the wing are different.

5.2.2. Effect of the initial phase angle From the above results for $Re \geqslant 120$, we find that the body goes upward, but the flight direction should depend on the initial phase ϕ of the flapping
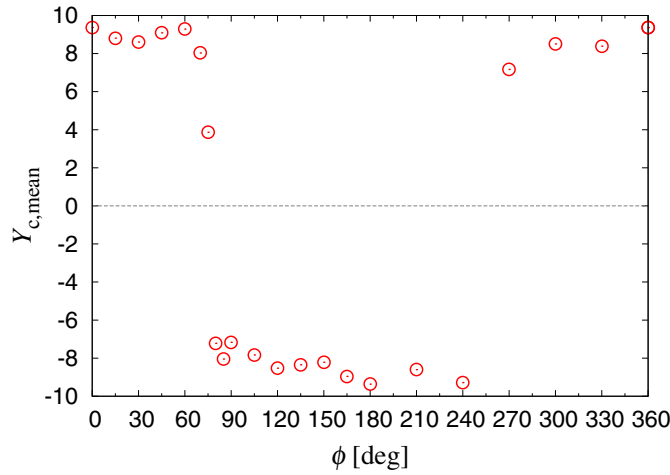
Figure 8. Time-averaged position $Y_{c,mean}$ for $12 \leqslant t/T \leqslant 13$ against the initial phase ϕ of $0^{\circ} \leqslant \phi < 360^{\circ}$ at $Re = 200$ under no gravity.
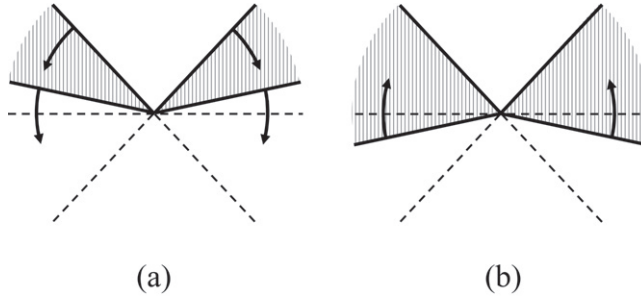

Figure 9. Range of initial phases where the upward flight is possible at $Re = 200$ under no gravity. (a) Down-stroke from the initial position of $0^{\circ} \leqslant \phi \leqslant 75^{\circ}$ and (b) up-stroke from the initial position of $255^{\circ} \leqslant \phi < 360^{\circ}$.

in (2.1). We next investigate the effect of the initial phase ϕ on flapping flight at $Re = 200$ under no gravity. Figure 8 shows the time-averaged position $Y_{c,mean}$ for $12 \leqslant t/T \leqslant 13$ against the initial phase ϕ in the range 0–360° at $Re = 200$ under no gravity. First of all, we obtain symmetric results satisfying the relation $Y_{c,mean}(\phi + 180^{\circ}) = -Y_{c,mean}(\phi)$. The results are reasonable and show the validity of the present numerical method. It is found from figure 8 that for $0^{\circ} \leqslant \phi \leqslant 75^{\circ}$ and $255^{\circ} \leqslant \phi < 360^{\circ}$ the body goes upward, while for other phase angles the body goes downward. The range of initial phases where the body goes upward is illustrated in figure 9.

5.2.3. Symmetry breaking of flows   We find from figure 7 that for $55 \leqslant Re \leqslant 110$ the body goes either upward or downward by the symmetry breaking of flows and that the direction of the motion depends on the disturbances. Note that for $Re \geqslant 65$ the body goes only upward by the effect of the initial condition of $\phi = 0^{\circ}$ if there is no disturbance. Here, we investigate how the symmetry breaking of flows appears at $Re = 90$ by focusing on the vorticity field ω $(= \partial v/\partial x - \partial u/\partial y)$. Figure 10 shows vorticity contours at each half stroke for the case of 'Disturbance (2%@$t/T = 3$)' at $Re = 90$ with $\phi = 0^{\circ}$ in figure 7 (i.e. for this case the body goes upward by the initial condition of $\phi = 0^{\circ}$ and the disturbance with $\alpha = 2$). As seen
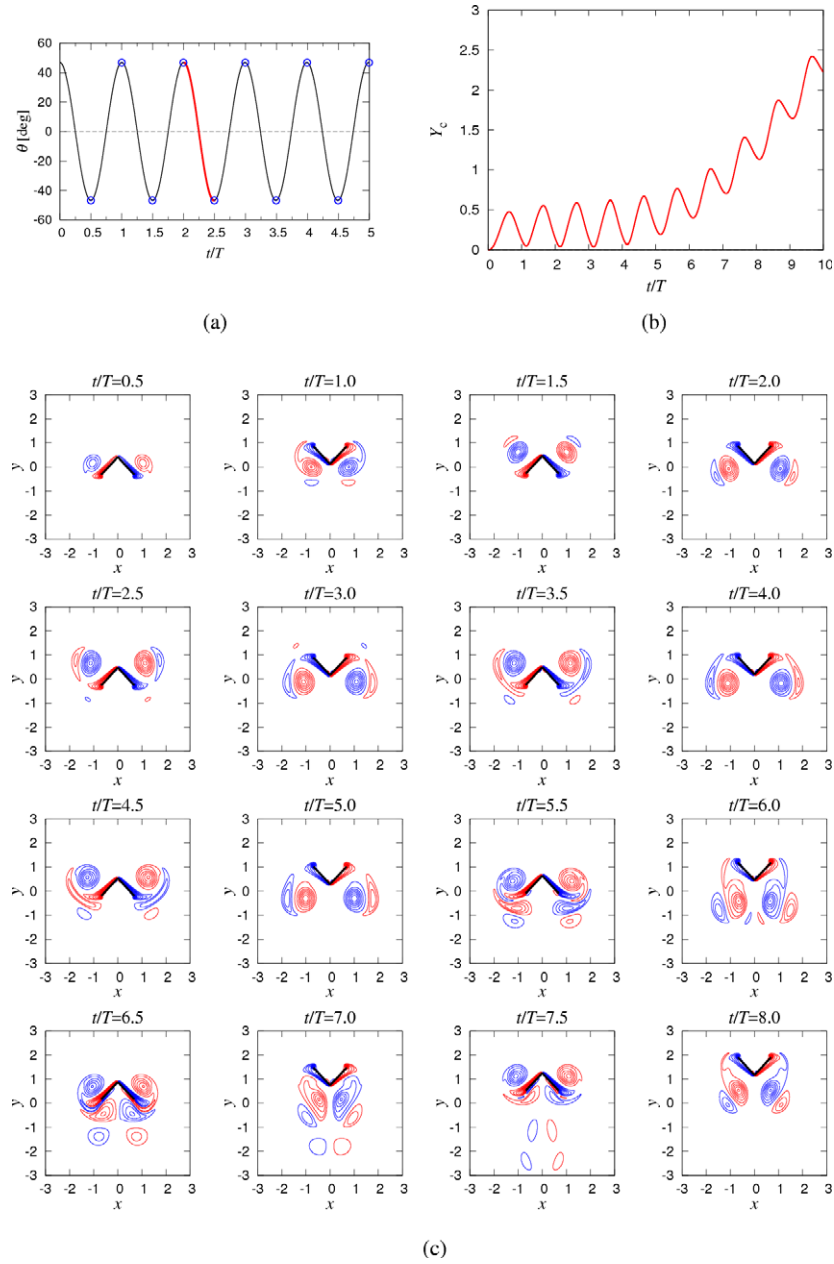
Figure 10. Vorticity contours around flapping wings under no gravity at $Re = 90$ with $\phi = 0^{\circ}$ for the case of 'Disturbance (2%@$t/T = 3$)' in figure 7: (a) angular position of the wing including a small disturbance for $2 \leqslant t/T \leqslant 2.49$, (b) trajectory of the body and (c) vorticity contours with the interval of $\omega = 2$; solid red and dashed blue lines denote positive and negative contours, respectively.

in figure 10, the LEVs newly created around the wings interact in a complicated manner with previously shed vortices, and the vorticity fields for $t/T \leqslant 4$ are almost symmetric with respect to the horizontal line, although a tiny asymmetric flow is already found. For $t/T \geqslant 4.5$, however, the vorticity fields gradually break symmetry, and an asymmetric flow
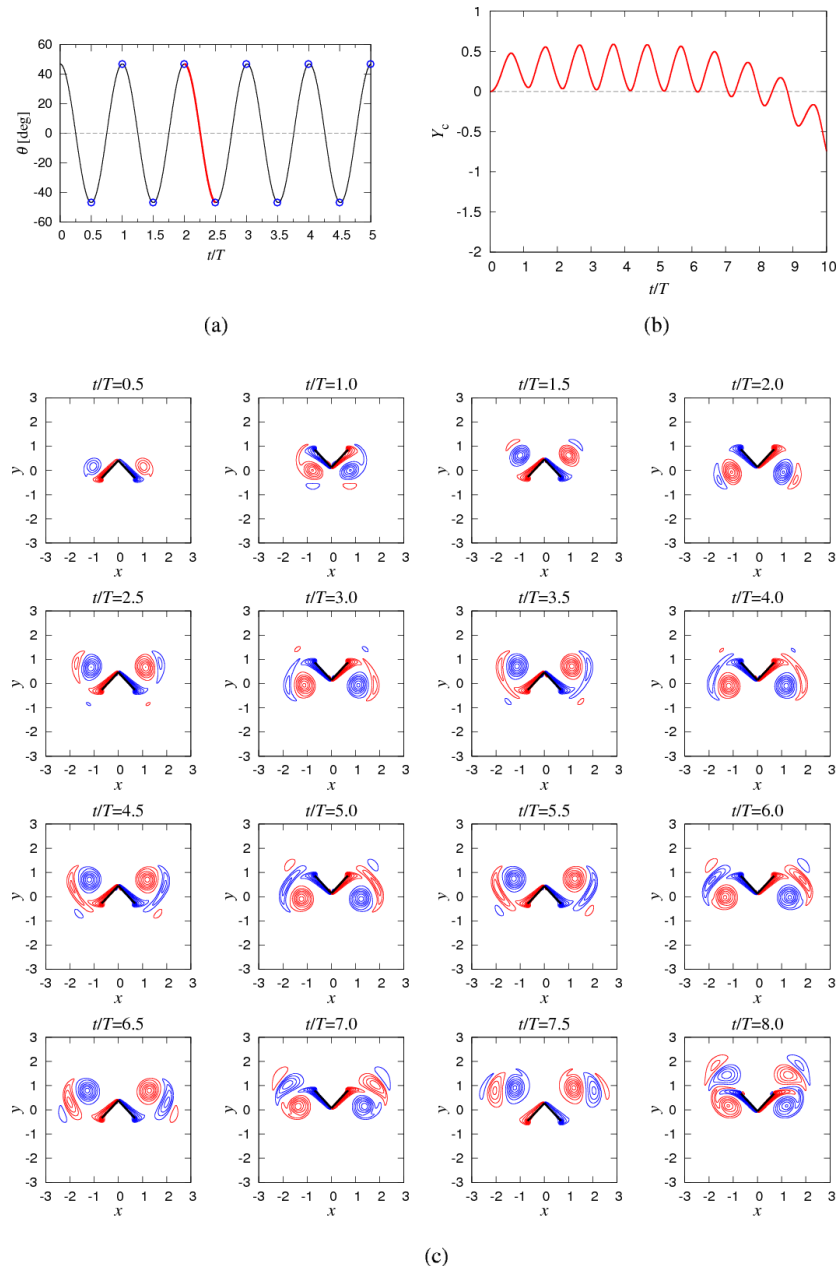
14

Figure 11. Vorticity contours around flapping wings under no gravity at $Re = 90$ with $\phi = 0°$ for the case of 'Disturbance $(-2\%@t/T = 3)$' in figure 7: (a) angular position of the wing including a small disturbance for $2 \leqslant t/T \leqslant 2.51$, (b) trajectory of the body and (c) vorticity contours with the interval of $\omega = 2$; solid red and dashed blue lines denote positive and negative contours, respectively.

clearly appears for $t/T \geqslant 5.5$. According to the symmetry breaking, the body goes upward after $t/T = 4.5$. On the other hand, figure 11 shows vorticity contours at each half stroke for the case of 'Disturbance $(-2\%@t/T = 3)$' at $Re = 90$ with $\phi = 0°$ in figure 7 (i.e. for
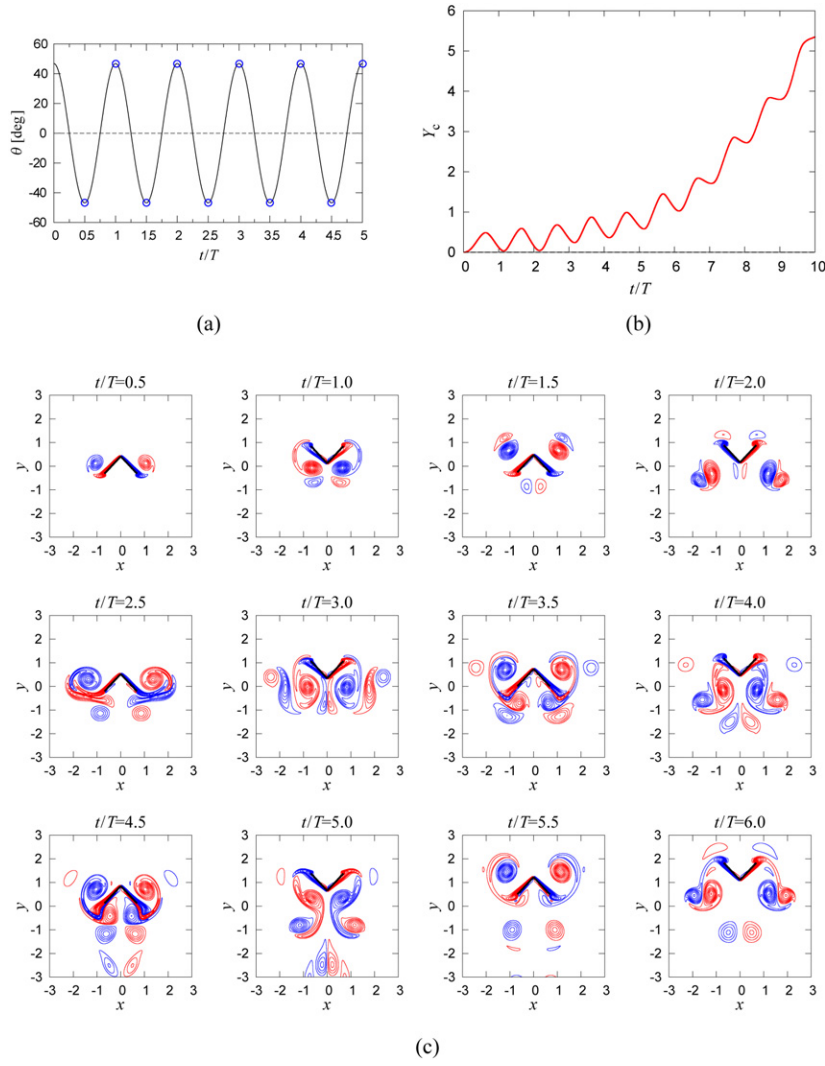
Figure 12. Vorticity contours around flapping wings under no gravity at $Re = 200$ with $\phi = 0^{\circ}$: (a) angular position of the wing, (b) trajectory of the body and (c) vorticity contours with the interval of $\omega = 2$; solid red and dashed blue lines denote positive and negative contours, respectively.

this case the body goes downward by the disturbance with $\alpha = -2$ overcoming the initial condition of $\phi = 0^{\circ}$). In this case, the vorticity fields for $t/T \leqslant 6.5$ are almost symmetric with respect to the horizontal line, and an asymmetric flow appears for $t/T \geqslant 7$. It is interesting that the vorticity field at $t/T = 7$ in figure 11 is similar to that at $t/T = 5.5$ in figure 10, if those are turned upside down, indicating that the symmetry breaking in this case is the opposite of the previous case. Therefore, the body goes downward in this case after $t/T \geqslant 7$. From these results at $Re = 90$, we find that a tiny asymmetric flow caused by the initial condition and/or the disturbance at the early stroke accumulates afterwards and finally large asymmetric flows appear.

We find from figure 7 that for $Re \geqslant 120$ the body goes upward in spite of the disturbances. We next investigate how the symmetry breaking of flows appear at $Re = 200$. Figures 12
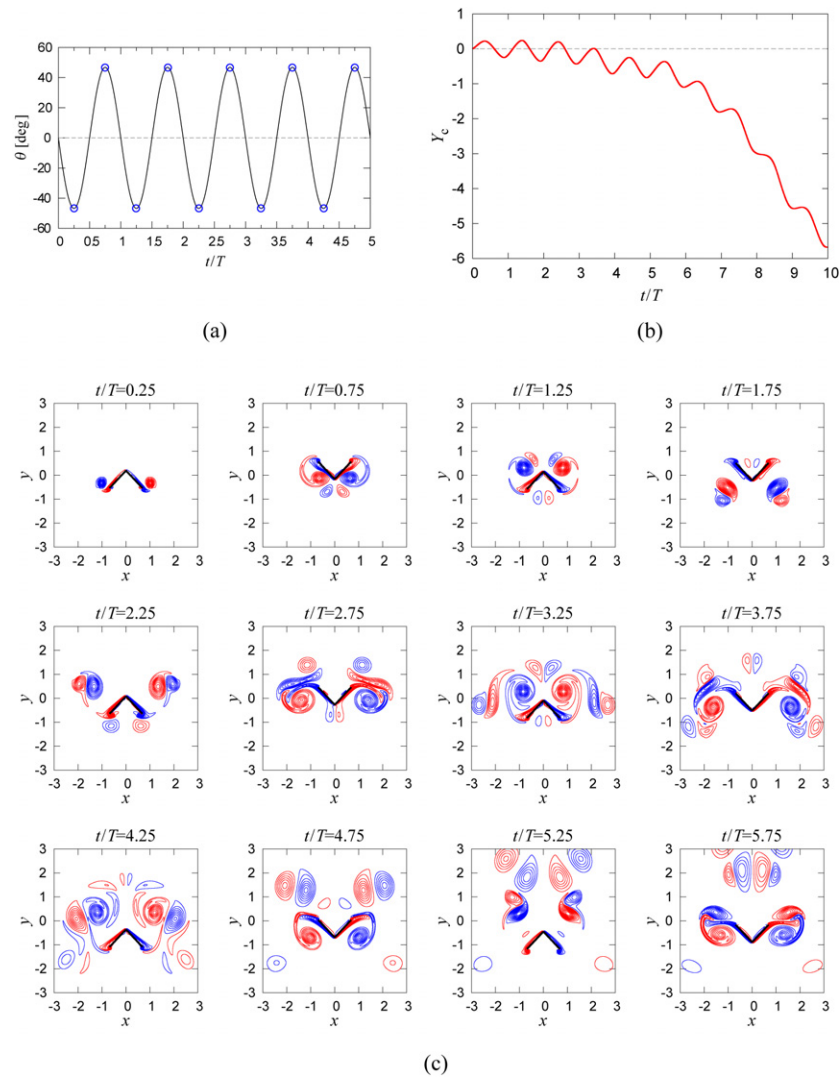
16

Figure 13. Vorticity contours around flapping wings under no gravity at $Re = 200$ with $\phi = 90^\circ$:
(a) angular position of the wing, (b) trajectory of the body and (c) vorticity contours with
the interval of $\omega = 2$; solid red and dashed blue lines denote positive and negative contours,
respectively.

and 13 show vorticity contours at $Re = 200$ with $\phi = 0^\circ$ and 90°, respectively. In these cases,
large asymmetric flows depending on the initial condition of ϕ appear in very early strokes.
Moreover, the vorticity field at $t/T = 2.5$ in figure 12 is very similar to that at $t/T = 2.75$
in figure 13 if those are turned upside down. Thus, the body goes in the opposite directions
depending on the initial phase angle ϕ of the wings.

From the comparison of the results in figures 10–13, it is seen that the accumulation
of the asymmetric flows becomes larger as the Reynolds number increases. Therefore, it
is considered that a history effect of flows (vortices are conserved for a long time at high
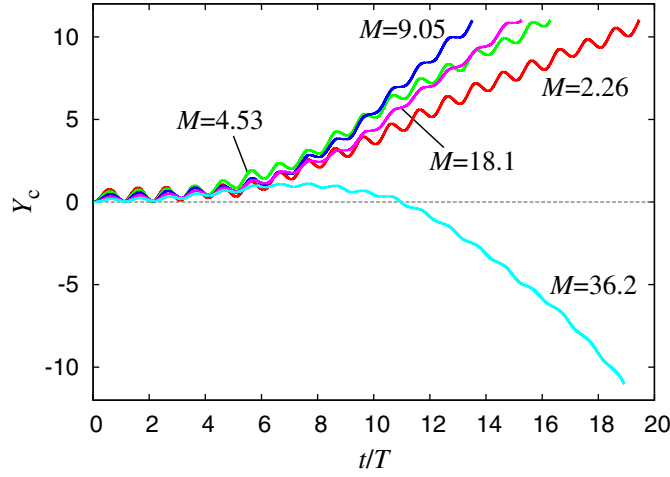Reynolds numbers) would cause symmetry breaking.

Figure 14. Trajectories of Y_c (the y-position of the center of mass) at $Re = 200$ with $\phi = 0°$ under no gravity for various values of mass M.
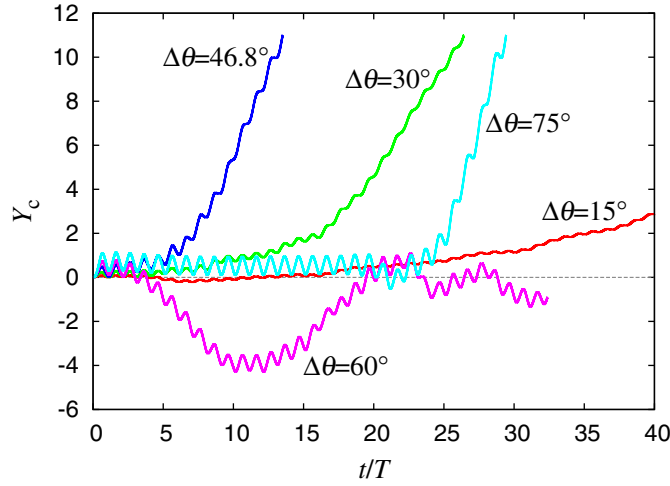

Figure 15. Trajectories of Y_c (the y-position of the center of mass) at $Re = 200$ with $\phi = 0°$ under no gravity for various values of the flapping amplitude $\Delta\theta$.

5.2.4. Effect of mass   Next, we investigate the effect of mass on flapping flight under no gravity. Figure 14 shows the trajectories of the body with different values of mass M at $Re = 200$ with $\phi = 0°$ and $\Delta\theta = 46.8°$. It is found that the body moves up and down more largely as the mass M decreases and that the body with $M = 9.05$ goes upward most quickly in the present cases. The body with $M = 36.2$ goes upward during early strokes, but downward after $t/T = 8$ when the vortices maintained under the wings move to the upper side of the wings due to the interaction of the vortices.

5.2.5. Effect of the flapping amplitude   The effect of the flapping amplitude is shown in figure 15. We use five flapping amplitudes of $\Delta\theta = \pi/12 (= 15°)$, $\pi/6 (= 30°)$, $2\pi \times 0.13$ $(= 46.8°)$, $\pi/3 (= 60°)$ and $5\pi/12 (= 75°)$ at $Re = 200$ with $\phi = 0°$. We find from figure 15
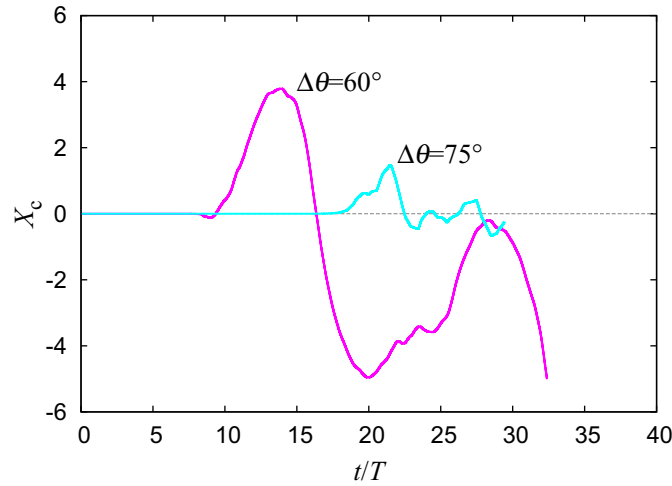
Figure 16. Trajectories of X_c (the *x*-position of the center of mass) at $Re = 200$ with $\phi = 0°$ under no gravity for various values of the flapping amplitude $\Delta\theta$.
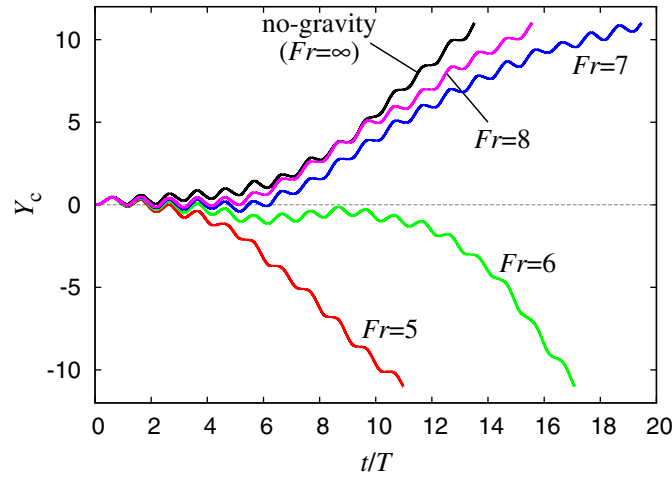

Figure 17. Trajectories of Y_c (the *y*-position of the center of mass) at $Re = 200$ with $\phi = 0°$ under gravity for various Froude numbers.

that the body goes upward more quickly as the amplitude increases up to $\Delta\theta = 46.8°$. For $\Delta\theta = 60°$ and $75°$, however, the body moves along a strange trajectory not only in the *y*-direction but also in the *x*-direction, as shown in figure 16. If the body moves in both the *x*- and *y*-directions, we should take into account the rotational motion of the body, which is ignored in the present study. The study on the rotational motion of the body is left for future work. The above-described results indicate an interesting fact that larger amplitudes do not work well for flapping flight, and there exists an appropriate amplitude of the flapping wings.

5.3. Flapping flight under gravity

Finally, we compute flapping flight under gravity for $\phi = 0°$ and $60 \leqslant Re \leqslant 300$. We change the Froude number in the range of 3–60 in order to investigate the effect of gravity on
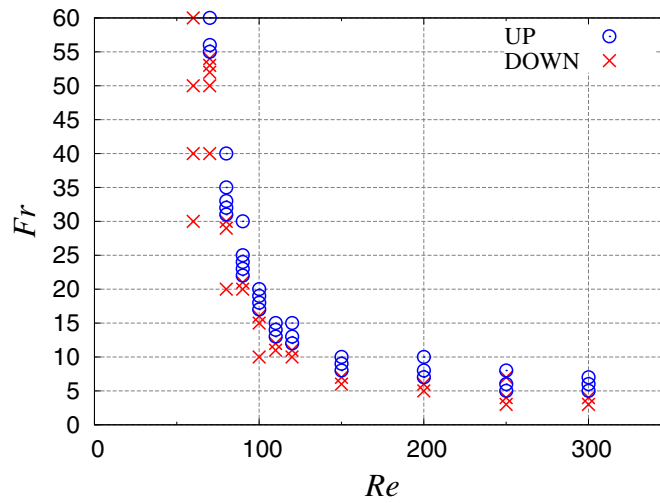
Figure 18. Upward and downward flight on the *Re–Fr* plane. The initial phase is $\phi = 0°$.

flapping flight. Note that no disturbance is applied to the motion of the wings in the following computations. Figure 17 shows flapping flights at $Re = 200$ for various Froude numbers. It is found from the figure that the body goes upward for $Fr \geqslant 7$ and as the Froude number increases, the upward velocity U_c increases. Also, looking at the trajectories in the five early strokes, we note that after the body moves upward by the first half stroke, it goes downward very slowly by gravity in spite of Fr. The same simulations are carried out for other Reynolds numbers, and the results are shown in figure 18. It is seen that as the Reynolds number increases, the critical Froude number over which the upward flapping flight is possible decreases. It is noted that at $Re = 60$ the upward flapping flight is impossible for $Fr \leqslant 60$. The boundary between the upward and the downward flight looks like a hyperbolic curve for $70 \leqslant Re \leqslant 200$. For $Re \geqslant 250$ the motion of the body becomes complicated due to the vortices reflected on the outer walls, and $F_x \neq 0$ and $X_c \neq 0$. For these cases, we should take into account the rotational motion of the body in future work.

In addition, since we get the relation $Fr/Re = \hat{\nu}/\sqrt{\hat{G}\hat{L}^3}$ from the definitions (3.3) and (3.6), Fr and Re cannot be changed independently in practice. For example, if we consider flight in the air on the earth where $\hat{\nu}$ and $\hat{G}$ are given, we get the relation $Fr = C Re$ where C is a constant that depends only on $\hat{L}$. Therefore, we should note that Fr and Re are changed with the time-averaged tip speed $\bar{\hat{u}}_{\text{tip}}$ (which is determined by $\hat{T}$ with given $\hat{L}$ and $\Delta\theta$) along a straight line $Fr = C Re$ through the origin in figure 18, and the critical $\bar{\hat{u}}_{\text{tip}}$ over which the flapping flight is possible is determined by the intersecting point of the straight line ($Fr = C Re$) with the hyperbola-like curve (the boundary between the upward and the downward flight) in figure 18.

6. Conclusions

We have applied the IB-LBM to the investigation of 2D symmetric flapping flight.

Firstly, we investigated the effect of the Reynolds number in the range of 40–200 on flows around symmetric flapping wings initially located at the most upward position under no gravity field and found that for high Reynolds numbers ($Re \geqslant 55$), asymmetric vortices with respect to the horizontal line appear and the time-averaged lift force is induced on the

wings, whereas for low Reynolds numbers ($Re \leqslant 50$), only symmetric vortices appear around the wings and no lift force is induced. In addition, we found the bistable phenomena for $55 \leqslant Re \leqslant 110$ where the body goes either upward or downward depending on disturbances. For $Re \geqslant 120$, the body goes upward in spite of disturbances less than 5%. The symmetry breaking of flows was investigated by focusing on vorticity fields, and it was found that the symmetry breaking is caused by a history effect of flows.

Secondly, the effect of the initial position of the wings was investigated, and the range of the initial phase where the upward flight is possible was found. The effects of the mass and the flapping amplitude were also studied, and we found that there exist appropriate values of the mass and of the amplitude of the flapping wings for efficient flight.

Finally, we carried out free flight simulations under gravity field for various Reynolds and Froude numbers and found the region where upward flight is possible. As the Reynolds number increases, the critical Froude number over which the upward flapping flight is possible decreases. The boundary between the upward and the downward flight becomes a hyperbolic curve for $70 \leqslant Re \leqslant 200$.

The studies of the rotational motion of the body, asymmetric flapping wings and 3D flapping wings are left for future work. The behavior for higher Reynolds numbers over 10^3 is also interesting.

Acknowledgments

Appendix A. Non-dimensional variables

In section 3, we use the following non-dimensional variables defined by the wing length $\hat{L}$, the time-averaged tip speed $\overline{\hat{u}}_{\text{tip}}$ and a reference fluid density $\hat{\rho}_0$:

$$\left.\begin{aligned}
\boldsymbol{x} &= \hat{\boldsymbol{x}}/\hat{L}, & \boldsymbol{u} &= \hat{\boldsymbol{u}}/\overline{\hat{u}}_{\text{tip}}, \\
t &= \hat{t}\,\overline{\hat{u}}_{\text{tip}}/\hat{L}, & p &= \hat{p}/(\hat{\rho}_0\overline{\hat{u}}_{\text{tip}}^2), \\
\boldsymbol{X}_{\text{c}} &= \hat{\boldsymbol{X}}_{\text{c}}/\hat{L}, & \boldsymbol{U}_{\text{c}} &= \hat{\boldsymbol{U}}_{\text{c}}/\overline{\hat{u}}_{\text{tip}}, \\
M &= \hat{M}/(\hat{\rho}_0\hat{L}^2), & \boldsymbol{F} &= \hat{\boldsymbol{F}}/(\hat{\rho}_0\overline{\hat{u}}_{\text{tip}}^2\hat{L}), \\
\boldsymbol{G} &= \hat{\boldsymbol{G}}\hat{L}/\overline{\hat{u}}_{\text{tip}}^2.
\end{aligned}\right\} \tag{A.1}$$

Note that the circumflex represents 'dimensional'.

In sections 4 and 5, we use the following non-dimensional variables:

$$\left.\begin{aligned}
c_i &= \hat{c}_i/\hat{c}, & \boldsymbol{x} &= \hat{\boldsymbol{x}}/\hat{L}, & t &= \hat{t}\,\overline{\hat{u}}_{\text{tip}}/\hat{L}, \\
f_i &= \hat{f}_i/\hat{\rho}_0, & \rho &= \hat{\rho}/\hat{\rho}_0, & \boldsymbol{u} &= \hat{\boldsymbol{u}}/\hat{c}, \\
p &= \hat{p}/(\hat{\rho}_0\hat{c}^2), & \nu &= \hat{\nu}/(\hat{c}\hat{L}), & \boldsymbol{g} &= \hat{\boldsymbol{g}}\hat{L}/(\hat{\rho}_0\hat{c}^2), \\
\boldsymbol{X}_k &= \hat{\boldsymbol{X}}_k/\hat{L}, & \boldsymbol{U}_k &= \hat{\boldsymbol{U}}_k/\hat{c}, \\
\boldsymbol{X}_{\text{c}} &= \hat{\boldsymbol{X}}_{\text{c}}/\hat{L}, & \boldsymbol{U}_{\text{c}} &= \hat{\boldsymbol{U}}_{\text{c}}/\hat{c}, \\
M &= \hat{M}/(\hat{\rho}_0\hat{L}^2), & \boldsymbol{F} &= \hat{\boldsymbol{F}}/(\hat{\rho}_0\hat{c}^2\hat{L}), & \boldsymbol{G} &= \hat{\boldsymbol{G}}\hat{L}/\hat{c}^2,
\end{aligned}\right\} \tag{A.2}$$

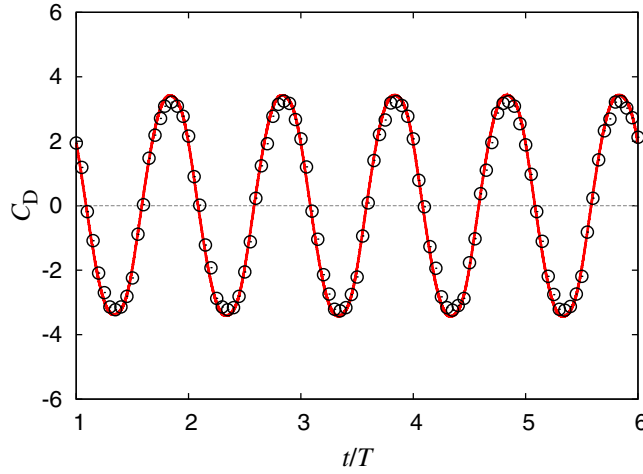where $\hat{c}$ is a characteristic particle speed.

Figure B.1. Time variation of the drag coefficient C_D of a laterally oscillating circular cylinder at $Re = 100$ with $KC = 5$: solid line, the present result; $\circ$, numerical results of Dütsch *et al* (1998).

Appendix B. Validation of the numerical method

B.1. The oscillating circular cylinder

In order to examine the accuracy of the present method, we have calculated the flow induced by an oscillating circular cylinder in a stationary fluid by the IB-LBM. The diameter of the cylinder is D, and the width and height of the computational domain are $55D$ and $35D$, respectively. The cylinder placed at the center of the domain oscillates laterally with the following speed:

$$U_c(t) = -U_{\max} \cos\left(\frac{2\pi}{T}t\right), \tag{B.1}$$

where $U_c(t)$ is the velocity component in the x-direction of the cylinder, $U_{\max}$ is the amplitude of the velocity and T is the period. In the computations, the grids of $D = 50\Delta x$ and $U_{\max} = 0.02$ are used, and the Neumann condition is applied at the outer boundary of the domain. Note that since $\boldsymbol{U}_c$ and $\boldsymbol{X}_c$ are given in this case, we do not need to compute them by (4.23) and (4.24). In addition, the force acting on the cylinder can be computed by adding the internal mass effect inside the cylinder (Suzuki and Inamuro 2011) to the force obtained by (4.22). The flow is determined by the parameters of the Keulegan–Carpenter (KC) number and the Reynolds number, and we set $KC = U_{\max}T/D = 5$ and $Re = U_{\max}D/\nu = 100$. Figure B.1 shows the time variation of the drag coefficient $C_D = F_x/(\frac{1}{2}\rho_0 U_{\max}^2 D)$. The result of the present method agrees well with the numerical results of Dütsch *et al* (1998).

B.2. The impulsively moving circular cylinder

The second problem is a flow around a circular cylinder started impulsively from rest and translated at a constant speed. The diameter of the cylinder is D, and the computational domain is $30D \times 30D$ with the no-slip boundary condition at the the outer boundary of the domain. The cylinder is placed at $(16.5D, 15D)$ and impulsively translated to the left with a constant speed of U_c. We compute the drag force F_x acting on the cylinder for $Re = U_c D/\nu = 40$ and 200 by the IB-PLBM with $D = 60\Delta x$ and $90\Delta x$ for $Re = 60$ and 200,
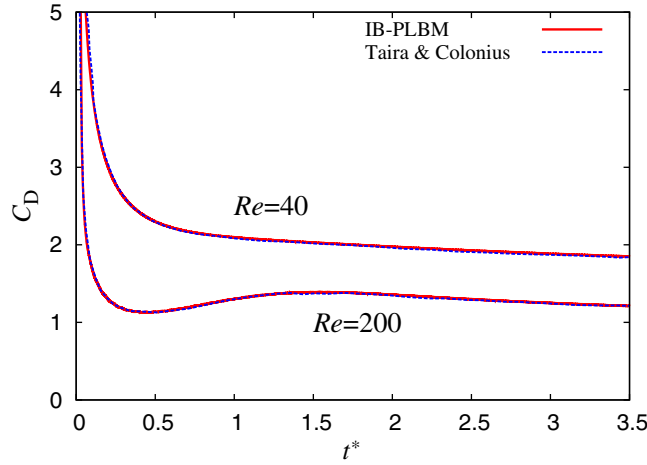
22

Figure B.2. Time variation of the drag coefficient C_D of an impulsively moving circular cylinder at $Re = 40$ and 200 compared with the numerical results of Taira and Colonius (2007). $t^* = tU_c/D$.
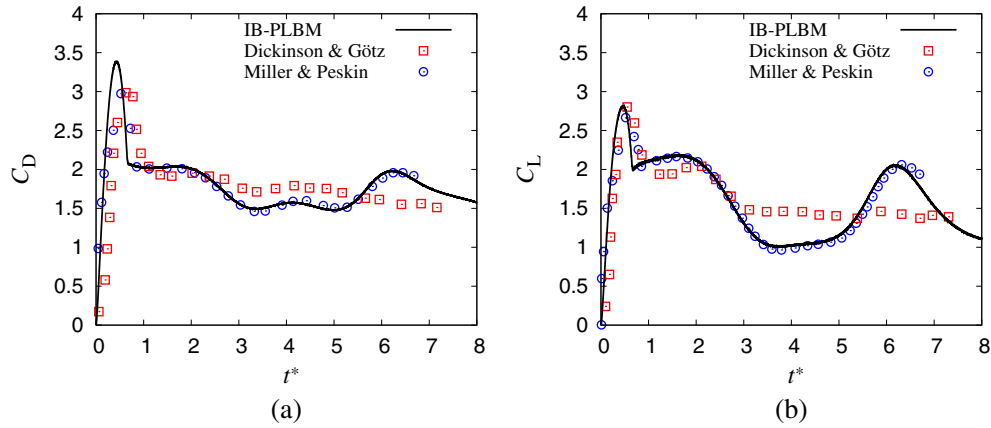

Figure B.3. Time variations of (a) the drag coefficient C_D and (b) the lift coefficient C_L of an almost impulsively moving plate with the angle of attack $\Lambda = 45°$ at $Re = 192$ compared with the experimental results of Dickinson and Götz (1993) and with the numerical results of Miller and Peskin (2004). $t^* = tU_0/L$.

respectively, and $U_c = 0.01$. The iteration for solving the Poisson equation (4.13) is repeated until $|p_{n+1} - p_n| < 10^{-10}$ is satisfied in the whole domain. Figure B.2 shows the time variation of the drag coefficient $C_D = F_x/(\frac{1}{2}\rho_0 U_c^2 D)$ compared with the numerical solutions of Taira and Colonius (2007). The results of the present method agree quite well with their numerical results for $Re = 40$ and 200.

B.3. The almost impulsively moving plate

The third problem is a flow around an inclined plate (the angle of attack $\Lambda = 45°$) started almost impulsively from rest and translated at a constant speed. The length of the plate is L, and the width and height of the computational domain are $20L$ and $8L$, respectively. The no-slip boundary condition is used at the outer boundary of the domain. The inclined plate
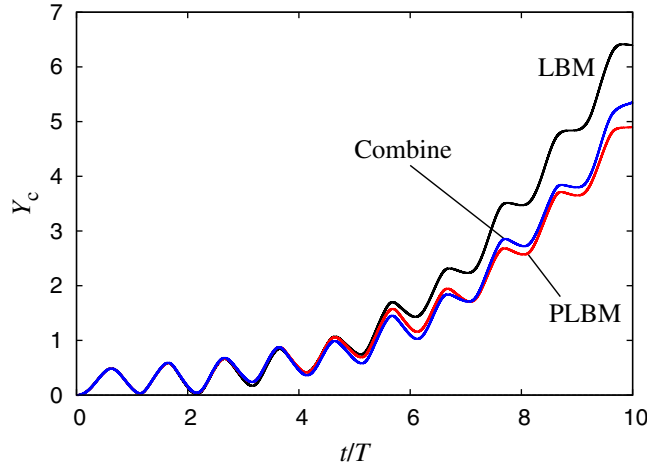
Figure C.1. Trajectories of Y_c (the y-position of the center of mass) at $Re = 200$ with $\phi = 0°$ under no gravity by the IB-LBM, the IB-PLBM and the combination of the IB-LBM and the IB-PLBM.
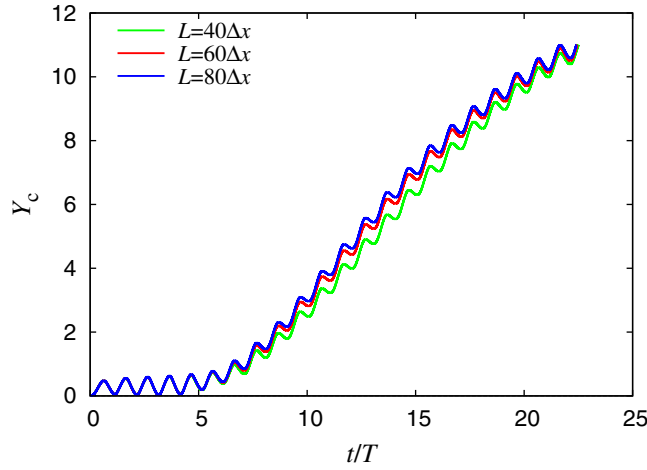

Figure D.1. Trajectories of Y_c (the y-position of the center of mass) at $Re = 100$ with $\phi = 0°$ under no gravity with three different grids.

is placed at $(7.5L, 4L)$ and almost impulsively translated to the right with a speed of $U_c(t)$ given by

$$U_c(t) = \begin{cases} \frac{1}{2}U_0 \left[1 + \cos\left(\pi + \frac{\pi t}{\Delta t_{trans}}\right)\right], & 0 \leqslant t \leqslant \Delta t_{trans}, \\ U_0, & \Delta t_{trans} < t. \end{cases} \quad (B.2)$$

We compute the drag force F_x and the lift force F_y acting on the plate for $Re = U_0 L/\nu = 192$ with $U_0 \Delta t_{trans}/L = 0.65$ by the IB-PLBM with $L = 60\Delta x$ and $U_0 = 0.02$. The iteration for solving the Poisson equation (4.13) is repeated until $|p_{n+1} - p_n| < 10^{-9}$ is satisfied in the whole domain. Figure B.3 shows time variations of the drag and the lift coefficient, $C_D = -F_x/(\frac{1}{2}\rho_0 U_0^2 L)$ and $C_L = F_y/(\frac{1}{2}\rho_0 U_0^2 L)$, compared with the experimental results of Dickinson and Götz (1993) and with the numerical results of Miller and Peskin (2004). The results of the present method agree well with those of Miller and Peskin (2004).

Table E.1. Typical computational conditions in section 5. $\overline{u}_{\text{tip}}$ is determined by the relation $\overline{u}_{\text{tip}} T/\Delta t = 4L\Delta\theta/\Delta x$.

No.	Re	Fr	$L/\Delta x$	τ	$T/\Delta t$	$\overline{u}_{\text{tip}}$	G
1	40	∞	60	0.5420	21000	0.009 335	0
2	50	∞	60	0.5336	21000	0.009 335	0
3	100	∞	60	0.5168	21000	0.009 335	0
4	150	∞	60	0.5112	21000	0.009 335	0
5	200	∞	80	0.5112	28000	0.009 335	0
6	70	52	60	0.5240	21000	0.009 335	3.223×10^{-8}
7	70	53	60	0.5240	21000	0.009 335	3.102×10^{-8}
8	70	54	60	0.5240	21000	0.009 335	2.988×10^{-8}
9	70	55	60	0.5240	21000	0.009 335	2.881×10^{-8}
10	80	29	60	0.5210	21000	0.009 335	1.036×10^{-7}
11	80	30	60	0.5210	21000	0.009 335	9.683×10^{-8}
12	80	31	60	0.5210	21000	0.009 335	9.068×10^{-8}
13	80	32	60	0.5210	21000	0.009 335	8.510×10^{-8}
14	90	20	60	0.5187	21000	0.009 335	2.179×10^{-7}
15	90	21	60	0.5187	21000	0.009 335	1.976×10^{-7}
16	90	22	60	0.5187	21000	0.009 335	1.800×10^{-7}
17	90	23	60	0.5187	21000	0.009 335	1.647×10^{-7}
18	100	15	60	0.5168	21000	0.009 335	3.873×10^{-7}
19	100	16	60	0.5168	21000	0.009 335	3.404×10^{-7}
20	100	17	60	0.5168	21000	0.009 335	3.015×10^{-7}
21	100	18	60	0.5168	21000	0.009 335	2.690×10^{-7}
22	150	6	60	0.5112	21000	0.009 335	2.421×10^{-6}
23	150	7	60	0.5112	21000	0.009 335	1.778×10^{-6}
24	150	8	60	0.5112	21000	0.009 335	1.362×10^{-6}
25	150	9	60	0.5112	21000	0.009 335	1.076×10^{-6}
26	200	5	80	0.5112	28000	0.009 335	3.486×10^{-6}
27	200	6	80	0.5112	28000	0.009 335	2.421×10^{-6}
28	200	7	80	0.5112	28000	0.009 335	1.778×10^{-6}
29	200	8	80	0.5112	28000	0.009 335	1.362×10^{-6}
30	300	3	120	0.5112	42000	0.009 335	9.683×10^{-6}
31	300	4	120	0.5112	42000	0.009 335	5.446×10^{-6}
32	300	5	120	0.5112	42000	0.009 335	3.486×10^{-6}
33	300	6	120	0.5112	42000	0.009 335	2.421×10^{-6}

Appendix C. Comparison of the IB-LBM, the IB-PLBM and the combination of the IB-LBM and IB-PLBM

We compare the trajectories of the body at $Re = 200$ with $\phi = 0^{\circ}$ under no gravity by the IB-LBM, the IB-PLBM and the combination of the IB-LBM and IB-PLBM in figure C.1. In the combination of the IB-LBM and IB-PLBM, the IB-PLBM is used for $0 < t/T \leqslant 1$ and the IB-LBM is used for $t/T \geqslant 1$. At $t/T = 1$ the final results of f_i^{PLBM} by the IB-PLBM are transferred into the initial data of f_i^{LBM} for the IB-LBM so that the pressure p and the velocity $\boldsymbol{u}$ are correctly preserved as follows:

$$f_i^{\text{LBM}} = f_i^{\text{PLBM}} + E_i \left[\left(3p - \sum_{i=1}^{9} f_i^{\text{PLBM}} \right) + 3(3p - 1)\boldsymbol{c}_i \cdot \sum_{i=1}^{9} f_i^{\text{PLBM}} \boldsymbol{c}_i \right]. \quad (\text{C.1})$$
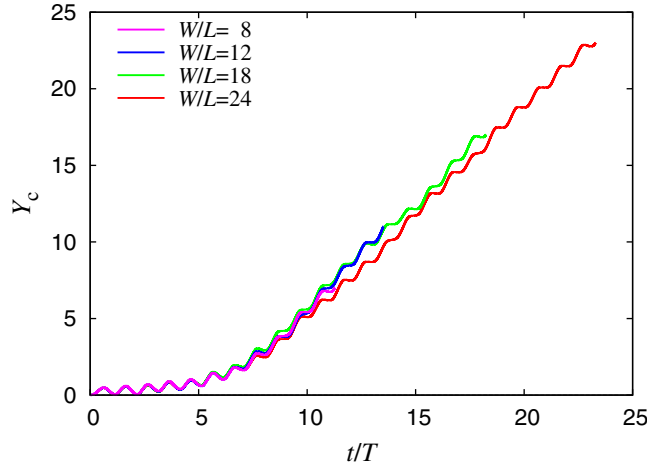
Figure F.1. Trajectories of Y_c (the *y*-position of the center of mass) at $Re = 200$ with $\phi = 0^\circ$ under no gravity with four different sizes of the computational domain.

In principle, the result of the IB-PLBM is most accurate, but the computation time by the IB-PLBM is much larger than those by the IB-LBM and the combination of the IB-LBM and IB-PLBM. The difference between the result of the IB-PLBM and those of the combination of the IB-LBM and IB-PLBM in the figure is quite small if these results are compared with the results at $Re = 200$ in figure 7, where the time-averaged position of the body considerably depends on small disturbances. Therefore, in order to save computation time, we use the combination of the IB-LBM and IB-PLBM in section 5.

Appendix D. Dependence of grid resolution

The dependence of grid resolution is examined by computing the trajectories of the body at $Re = 100$ with $\phi = 0^\circ$ under no gravity with three different grids of $L = 40\Delta x$, $60\Delta x$ and $80\Delta x$ as shown in figure D.1. It is seen that the results with $L = 60\Delta x$ and $80\Delta x$ almost coincide, while the result with $L = 40\Delta x$ is a little different from the other results. According to these results, we use $L = 60\Delta x$ for $40 \leqslant Re \leqslant 150$, $L = 80\Delta x$ for $150 < Re \leqslant 200$ and $L = 120\Delta x$ for $250 \leqslant Re \leqslant 300$.

Appendix E. Computational conditions

Typical computational conditions in section 5 are listed in table E.1.

Appendix F. Effect of domain size

The effect of the computational domain size on the results is investigated by using four different sizes of the domain of $W \times H = 24L \times 48L$, $18L \times 36L$, $12L \times 24L$ and $8L \times 16L$. Figure F.1 shows the trajectories of Y_c (the *y*-position of the center of mass) at $Re = 200$ under no gravity with four different sizes of the computational domain. It is seen that the three results except with the largest domain are in good agreement, and the result with the largest domain is a little different from the other results, but shows almost the same behavior.

As a result, the effect of the domain size is considered to be very small; thus the domain of $W \times H = 12L \times 24L$ is used in this study.

References

Alben S and Shelley M. 2005 Coherent locomotion as an attracting state for a free flapping body *Proc. Natl Acad. Sci. USA* **102** 11163–6

Dickinson M H and Götz K G 1993 Unsteady aerodynamic performance of model wings at low Reynolds numbers *J. Exp. Biol.* **174** 45–64

Dütsch H, Durst F, Becker S and Lienhart H 1998 Low Reynolds-number flow around an oscillating circular cylinder at low Keulegan–Carpenter numbers *J. Fluid Mech.* **360** 249–71

Feng Z-G and Michaelides E E 2005 Proteus: a direct forcing method in the simulations of particulate flows *J. Comput. Phys.* **202** 20–51

Iima M and Yanagita T 2001a An analysis of a symmetric flapping model: a symmetry-breaking mechanism and its universality *Theor. Appl. Mech.* **50** 237–45

Iima M and Yanagita T 2001b Is a two-dimensional butterfly able to fly by symmetric flapping? *J. Phys. Soc. Japan* **70** 5–8

Iima M and Yanagita T 2005 Asymmetric motion of a two-dimensional symmetric flapping model *Fluid Dyn. Res.* **36** 407–25

Iima M and Yanagita T 2006 A transition of ascending flight to vertical hovering: a study of a symmetric flapping model *Europhys. Lett.* **74** 55–61

Inamuro T, Ogata T, Tajima S and Konishi N 2004 A lattice Boltzmann method for incompressible two-phase flows with large density differences *J. Comput. Phys.* **198** 628–44

Inamuro T 2006 Lattice Boltzmann methods for viscous fluid flows and for two-phase fluid flows *Fluid Dyn. Res.* **38** 641–59

Junk M, Klar A and Luo L-S 2005 Asymptotic analysis of the lattice Boltzmann equation *J. Comput. Phys.* **210** 676–04

Lai M-C and Peskin C S 2000 An immersed boundary method with formal second-order accuracy and reduced numerical viscosity *J. Comput. Phys.* **160** 705–19

Miller L A and Peskin C S 2004 When vortices stick: an aerodynamic transition in tiny insect flight *J. Exp. Biol.* **207** 3073–88

Mittal R and Iaccarino G 2005 Immersed boundary methods *Annu. Rev. Fluid Mech.* **37** 239–61

Peskin C S 1972 Flow pattern around heart valves: a numerical method *J. Comput. Phys.* **10** 252–71

Sane S P 2003 The aerodynamics of insect flight *J. Exp. Biol.* **206** 4191–208

Shu C, Liu N and Chew Y T 2007 A novel immersed boundary velocity correction-lattice Boltzmann method and its application to simulate flow past a circular cylinder *J. Comput. Phys.* **226** 1607–22

Succi S 2001 *The Lattice Boltzmann Equation for Fluid Dynamics and Beyond* (Oxford: Oxford University Press)

Suzuki K and Inamuro T 2011 Effect of internal mass in the simulation of a moving body by the immersed boundary method *Comput. Fluids* **49** 173–87

Taira K and Colonius T 2007 The immersed boundary method: a projection approach *J. Comput. Phys.* **225** 2118–37

Vandenberghe N, Zhang J and Childress S 2004 Symmetry breaking leads to forward flapping flight *J. Fluid Mech.* **506** 147–55

Wang Z J 2005 Dissecting insect flight *Annu. Rev. Fluid Mech.* **37** 183–210

Wang Z, Fan J and Luo K 2008 Combined multi-direct forcing and immersed boundary method for simulating flows with moving particles *Int. J. Multiph. Flow* **34** 283–302